Ocean Science
Discussions

Open Access

On the modulation of the periodicity of the Faroe Bank Channel overflow instabilities

E. Darelius[1], I. Fer[1], T. Rasmussen[2], C. Guo[1], and K. M. H. Larsen[3]

[1]Geophysical Institute, University of Bergen and Bjerknes Centre for Climate Research, Bergen, Norway
[2]Danish Meteorological Institute, Copenhagen, Denmark
[3]Havstovan, Torshavn, Faroe Islands

Correspondence to: E. Darelius (elin.darelius@uib.no)

Title Page

Abstract · Introduction

Conclusions · References

Tables · Figures

◄ · ►

◄ · ►

Back · Close

Full Screen / Esc

Printer-friendly Version

Interactive Discussion

Abstract

The Faroe Bank Channel (FBC) is one of the major pathways where dense, cold water formed in the Nordic Seas flows southward towards the north Atlantic. The plume region downstream of the FBC sill is characterized by high mesoscale variability, quasi-regular oscillations and intense mixing. Here, one year-long time series of velocity and temperature from eight moorings deployed in May 2012 in the plume region is analyzed to describe variability in the strength and period of the oscillations. The eddy kinetic energy (EKE) associated with the oscillations is modulated with a factor of ten during the year and the dominant period of the oscillations changes between three to four and six days, where the shorter period oscillations are more energetic. The dense water is observed on a wider portion of the slope (both deeper and shallower) during periods with energetic, short period oscillations. The observations are complemented by results from a regional, high resolution model that shows a similar variability in EKE and a gradual change in oscillation period between three and four days. The observed variability in oscillation period is directly linked to changes in the volume transport across the sill: the oscillation period decreases with about six days Sv^{-1} both in the observations and in the model. This is in agreement with results from linear instability analysis which suggests that the period and growth rate decrease for decreased plume thickness. The changes in oscillation period can partly be explained by variability in the upper layer, background flow and advection of the oscillations past the stationary moorings, but the changes in the fraction of the EKE that is derived from the cross isobath motion suggests that the intrinsic period of the instability is modulated. It is further shown that about 50 % of the transport variability across the sill is explained by changes in the local barotropic forcing, which is obtained from satellite altimetry.

1 Introduction

The Faroe Bank Channel (FBC) is the deepest connection between the Nordic Seas and the North Atlantic, and it carries an outflow of about 2 Sv ($1\,\mathrm{Sv} \equiv 10^6\,\mathrm{m}^3\,\mathrm{s}^{-1}$) of cold, dense water formed north of the Greenland-Scotland ridge southwards (Hansen and Østerhus, 2007). Along its path, the overflowing water entrains and mixes with the overlying, ambient water (Mauritzen et al., 2005; Fer et al., 2010) and makes a substantial – up to 25 % – contribution to the formation of North Atlantic Deep Water (Dickson and Brown, 1994).

Mooring records from the overflow plume region downstream of the FBC sill show energetic mesoscale variability; the dense water is observed to advance along the slope in 100–200 m thick domes with a periodicity of 2–6 days (Darelius et al., 2011; Geyer et al., 2006). The domes are associated with a velocity signal extending throughout the water column and have a signature in the sea surface height (Darelius et al., 2013; Høyer and Quadfasel, 2001). Recent modeling efforts suggest that the oscillations are caused by growing baroclinic instabilities at the plume interface, manifested as topographic Rossby waves in the upper layer (Guo et al., 2014).

Mesoscale oscillations are not uncommon on the continental slopes of the North Atlantic/Nordic Seas; Miller et al. (1996) report on barotropic oscillations with a period of 1.8 days further west (12° W), on the southern side of the Iceland-Faroe Ridge, which they show to be wind-forced and linked to a resonant barotropic topographic Rossby normal mode. Further north, Mysak and Schott (1977) describe fluctuations in the Norwegian current with a periodicity of 2–3 days that they find to be caused by baroclinic instabilities. Skagseth and Orvik (2002) show that variability in the same frequency range (and the same region) agree with topographic waves of the first mode, while slightly longer periods (3–5 days) correspond to the second mode.

Oscillations – hereafter referred to as eddies – similar to those observed in the FBC overflow are frequently observed in other overflow regions; e.g. the Denmark Strait overflow (Krauss and Käse, 1998), and the Filchner overflow in Antarctica (Darelius

Title Page

Abstract | Introduction

Conclusions | References

Tables | Figures

|◀ | ▶|

◀ | ▶

Back | Close

Full Screen / Esc

Printer-friendly Version

Interactive Discussion

et al., 2009). The eddies modify vertical mixing and entrainment (Darelius et al., 2013), induce horizontal stirring (Voet and Quadfasel, 2010; Darelius et al., 2013) and influence the descent rate of the dense water (Seim et al., 2010). The intensity of eddy generation will thus affect the final properties and pathway of the overflow end product, the North Atlantic Deep Water.

Based on the first one year-long mooring record from the plume region (Ullgren et al., 2015), the modulation of the strength and in the dominant time scale of the mesoscale variability is described, and found to be substantially modulated throughout the year. The modulation of the oscillations and its coupling to oceanic and atmospheric forcing are explored and the analysis is extended to include results from a high resolution regional model (Rasmussen et al., 2014).

2 Data and methods

2.1 Moorings, 2012/13

Data were collected in the Faroe Bank Channel overflow region using eight bottom-anchored moorings in the period from 28 May 2012 to 5 June 2013 (Fig. 1). Three of the moorings were deployed in the channel (the C array), and five on the open slope about 80 km downstream of the sill (the S array and mooring M1). The moorings were equipped with temperature, conductivity and pressure recorders in addition to current meters. Further information on the moorings can be found in Ullgren et al. (2015) and in Table 1. The coordinate system for each mooring is aligned with the orientation of the corresponding mooring array, so that the x axis is perpendicular to the array and the y axis parallel to the array, pointing upslope. The angle of rotation is 34 and 31° (clockwise) for the C and S array respectively. Hourly mean data are interpolated to a grid with 1 m vertical resolution following the procedure outlined in Darelius et al. (2011). Velocity data from periods when the instrument tilt exceeds the acceptable threshold given by the manufacturer are excluded from the analysis. This

causes a slight bias towards lower velocities (since drag, and thus tilt, is larger for increasing velocities). The percentage of data discarded for any instrument is less than 3 %.

When the focus is on the evolution of the background field and not on the oscillations, the hourly data are filtered using a low-pass Butterworth filter of 4th order. The cut-off frequency is 30 days unless otherwise stated in the text where filtered data is discussed or shown.

Wavelet analysis is used to identify the dominant periods of variability and to describe how these change in time. The analysis is carried out using the hourly data and a Morlet mother function, and the 95 % significance level is found using a regular chi-square test (Torrence and Compo, 1997). The dominant oscillation period is defined as the period with highest, significant energy level at each time step.

The eddy kinetic energy (EKE) associated with the oscillations is estimated by integration using

$$\text{EKE} = \int_{f_1}^{f_2} (\Theta_u + \Theta_v)\, df, \tag{1}$$

where $f_1 = 1/6$ cycles per day (cpd), $f_2 = 2/5$ cpd, and $\Theta_{u/v}$ is the power spectral density in the along/across slope direction respectively. The presented EKE values are vertical means over the depth range with velocity measurements, see Table 1, except for S3 where only data from the upper Acoustic Doppler Current Profiler (ADCP), i.e. above the plume, are used. The EKE is normalized with the maximum value in respective time series. The EKE values are artificially elevated at the plume interface, since an instrument at a given level there is located alternatively in and out of the plume (see Ullgren et al., 2015). While it would be of interest to compare absolute EKE values from levels not affected by the plume, such are available only from S3. Time series of EKE is obtained by first calculating $\Theta_{u/v}$ in 30 day long, sliding windows. Integrating

Θ_v separately gives EKE_v, i.e. the EKE associated with motion in the across slope direction.

The transport, Q_T, of water colder than $T\,^{\circ}\text{C}$ past a mooring array is estimated from

$$Q_T(t) = \sum_{i=1}^{n} \int_0^{z_{i,T(t)}} u_i(z,t) L_i \, dz, \tag{2}$$

where n is the number of moorings in the array, u_i is the velocity perpendicular to the array at mooring i, $z_{i,T}$ the height of the $T\,^{\circ}\text{C}$ isotherm at mooring i, and L_i the representative width of the mooring. The distance between C1 and C2 is 7 km and the distance between C2 and C3 is 8 km and L is taken to be 7, 7.5 and 8 km for C1, C2 and C3, respectively. The transport values given are calculated using $T = 6\,^{\circ}\text{C}$, which roughly corresponds to $\sigma_\theta = 27.7\,\text{kg m}^{-3}$ and density range 3–5 in Mauritzen et al. (2005).

2.2 FBC-sill moorings

The mooring records from the plume region in 2012/13 described above are complemented with data from the long-term monitoring mooring from the FBC sill (Hansen and Østerhus, 2007). Moorings have been deployed quasi-continuously from 1995 until present at the location FB on the FBC sill (see Fig. 1 for location). Contemporary measurements from the sill (FB) and the plume region exist during the period June 2012–June 2013, when an upward looking ADCP (RD-Instruments 75 kHz BroadBand) was deployed at FB.

The data from FB consist of velocity profiles only, with no explicit information about the density of the overflowing water. Following the procedure outlined in Hansen and Østerhus (2007) the velocity profiles from FB are used to calculate the "kinematic overflow" volume flux. The upper boundary of the outflow is then set to be the level where the velocity is half the maximum outflow velocity.

2.3 Other data sets

Meteorological data (wind, pressure and temperature) from DMI are available from a weather station in Torshavn, Faroe Islands (Cappelen, 2014) with a temporal resolution of 3 h. Daily, gridded fields of sea level height anomalies (SLA) and geostrophic velocity anomalies calculated from satellite altimetry for the period and region of interest have been downloaded from http://www.aviso.altimetry.fr.

2.4 Numerical model

The model is a slightly modified version of the HYbrid Coordinate Ocean Model (HY-COM) v2.2.18 (Bleck, 2002; Chassignet et al., 2007). HYCOM exploits a hybrid coordinate system that is isopycnal in the open, stratified ocean, but smoothly reverts to a terrain-following coordinate in shallow coastal regions, and to z level coordinates in the mixed layer and/or unstratified seas. The vertical mixing is defined by the K-profile parameterization (KPP-scheme; Large et al., 1994). The horizontal grid size ranges from 750 to 1300 m and the resolution is highest near the Faroe Islands. This model setup has 32 vertical layers, 340 grid points in the southwest/northeast direction and 400 grid points in the southeast/northwest direction. The model domain is shown in Fig. 1. The bathymetry is extracted from ETOPO1 (Amante and Eakins, 2009) combined with measurements conducted by the Faroe Marine Research Institute (FAMRI) and the coast guard (Simonsen et al., 2002).

The barotropic velocities are prescribed on the boundary along with the sea surface height, whereas the baroclinic velocities, the temperature and the salinity are prescribed by a relaxation towards the boundary conditions (provided by a hindcast archive from the Danish Meterological Institut covering the Arctic and the North Atlantic Ocean) on the outermost 10 grid points. The time scale of relaxation on the boundary is one day, and decreases linearly to 10 days on the 10th grid point from the boundary. The atmospheric forcing is extracted from Era-Interim (2000–2009, Dee et al., 2011) and consists of the air temperature, short and long wave radiation, precipitation, wind

stress and the atmospheric vapor mixing ratio. The forcing is prescribed with a temporal resolution of 3 h and a spatial resolution of 79 km, which is interpolated to the model grid. Further details can be found in Rasmussen et al. (2014). In addition to the model output fields, time series for detailed analysis is extracted from a virtual mooring "M" on the slope (see Fig. 1).

3 Results

3.1 The FBC overflow plume

The FBC, located between the Faroe Plateau (FP) in the north and the Faroe Bank (FB) in the south, is about 840 m deep and less than 15 km wide at the sill. Results from the numerical model (Fig. 2) are used to illustrate the description of the FBC overflow plume. In the channel, the outflow forms a 200 m thick, cold layer leaning on the FP, with core velocities on the order of $1\,\mathrm{m\,s^{-1}}$ (Fig. 2a, e.g. Hansen and Østerhus, 2007; Hansen et al., 2001). The cold water continues to flow northwestward along the slope as a dense, gravity-driven plume that widens and thins as the channel opens up (Fig. 2b; Mauritzen et al., 2005). Downstream of the sill, baroclinic instabilities develop (Guo et al., 2014) and the dense plume breaks up into domes of cold water that are associated with eddies in the upper layer (Fig. 2c and d, Darelius et al., 2013). Following the procedure outlined in Bishop et al. (2013) and Guo et al. (2014), the divergent eddy heatflux (EHF) and the associated baroclinic conversion (BC) rate are calculated using one month long subsets of the HYCOM model results. Figure 2e and f show examples of EHF and BC-fields from August 2008, interpolated to 100 m above bottom (mab, fields are calculated in horizontal layers every 10th m in the vertical). The results are similar to those shown by Guo et al. (2014), with upslope divergent eddy heat fluxes and high baroclinic conversion rates ($BC \approx 10^{-5}\,\mathrm{m^2\,s^{-3}}$) appearing about 40–60 km downstream of the sill at the deeper edge of the dense plume.

3.2 Temporal evolution of mesoscale variability on the slope

The mooring records from the slope array show energetic oscillations in temperature and velocity with a period varying between 3 and 6 days (Fig. 3), similar to those described in Geyer et al. (2006); Darelius et al. (2011, 2013). While Geyer et al. (2006) stated that the oscillations were "highly regular", the present, longer observation records show that the intensity and the periodicity of the oscillations vary considerably in time. A direct inspection of the velocity records and wavelet analysis (Fig. 3d) suggests that the periods of oscillations alternate between three-four days and six days, where the low amplitude (i.e. less energetic) oscillations typically have longer periods. Based on the oscillation characteristics, the time series has been divided into six intervals, T1–6 (see Table 2–3 and Fig. 3). In all mooring locations, the EKE associated with the oscillations shows high values in August, January–February and in April, and a minimum in early winter (October–December, Fig. 3e). The intra-seasonal variability is large, e.g. at S3 the November EKE is only 10 % of the maximum value.

In the numerical model, the dominant periodicity of the oscillations is 3–4 days (Fig. 4a–d), similar to the observations. Unfortunately, a direct comparison is not possible because the model was not run for a period overlapping with the observations. The variability of the oscillations in the model, nevertheless, shows similarities with that in the observations: the EKE associated with the oscillations on the slope (at mooring M) varies by a factor of ten, with a minimum in March–April and a maximum in August–September (Fig. 4e). A comparison of Fig. 3d (observations) and Fig. 4d (model), however, shows that while the oscillations in the observations alternate between shorter (3–4 days) and longer (6 days) period, the change in period of the model oscillations is relatively gradual and appears to follow a seasonal cycle; it decreases from about four days in summer to about three days in November–December and then increases again to about 4 days towards the end of the record. Only once, in March, does the modeled oscillation period increase to about 6 days.

Figure 2f shows the baroclinic conversion (BC) rate associated with the oscillations in the numerical model. Time series of BC are constructed using the monthly mean value in an area (see Fig. 2) about 40–60 km downstream of the sill. The BC shows a maximum in August, and two minima: November and March (Fig. 4f). The time series of BC closely follows the EKE at M (Fig. 4e).

3.3 Modulation by the overflow at the sill

Time series of kinematic overflow measured at FB are shown in Fig. 5b together with the volume flux of water colder than $T = 6\,°C$ past array C (see Sect. 2.1 for calculation details). During the period with overlapping measurements, the low passed transport time series from FB and array C correlate well with a correlation coefficient of 0.9. The transport estimates from array C are lower by a factor of 0.84 compared with the kinematic overflow at FB. As discussed in e.g. Hansen and Østerhus (2007), the transport across the sill shows considerable variability on both daily and monthly time-scales. A relationship between the low passed (14 days) transport across the sill and the dominant period of the oscillations on the slope is apparent in Fig. 5a and further quantified in Fig. 6. Here, at each time step the dominant oscillation period (i.e. the oscillation period with the highest, significant energy level) from the wavelet analysis (shown in Figs. 3d and 5a) and the transport have been identified, and the transport is averaged in bins of oscillation period. Times of high transport coincide with shorter oscillation periods and times with low transport with longer oscillation periods. Linear regression gives a decrease in oscillation period of about $5.8\,\mathrm{days\,Sv^{-1}}$ for the observations.

The modeled transport Q across the sill displays a seasonal signal, increasing from 1 Sv in summer to 1.5 Sv in autumn (Fig. 4g). The observations from 2012/13 do not show a seasonal signal in transport, although a seasonality (of about the same amplitude but shifted in time with respect to the numerical model) emerges when combining all years of data from FB (Hansen and Østerhus, 2007, see their Fig. 23d). Repeating the analysis leading to the results shown in Fig. 6 using the model data gives a sensitivity similar to the observations ($-6.2\,\mathrm{days\,Sv^{-1}}$). The modeled transports, however,

are approximately 1 Sv lower than the observations. Note that longer period oscillations are only found during one short interval in the modeled time series.

The mean plume thickness, H, here defined as the height of the 6 °C isotherm, in the core of the plume on the slope (S2 and S3) shows variability (Fig. 3c) similar to the transport estimated from the mooring arrays in the channel (C and FB, Fig. 3b). The plume thickness recorded at S2 and S3 are typically in phase, implying that the variability is not caused by plume meandering. During periods with more intense oscillations and higher than normal plume thickness at S2 and S3 (T1 and T5), cold plume water is more often than normal present at the upper (S1) and lower (S4) mooring in the array (see Table 3). During T4, temperatures recorded by these moorings were above 3 °C at all times. A time series of monthly mean plume thickness (from the box marked in Fig. 2f) in the numerical model is shown in Fig. 4f. The mean plume thickness mimics the curves of EKE (Fig. 4e) and BC (Fig. 4f).

3.4 Currents in the upper layer

The modeled upper layer velocities (300 m depth) are shown in Fig. 7. Atlantic origin water flows northwestward along the Iceland-Faroe slope on the Faroe Plateau side. The current is stronger and extends further out from the shelf in August than in March. Meanwhile, there is a clockwise circulation around the Faroe Bank, causing a relatively strong shear across the FBC (a similar shear is observed in mooring data from the sill; Hansen and Østerhus, 2007). This current is also stronger in August than in March, when it has shifted westward following deeper isobaths and therefore to a lesser extent enters the FBC. In the model, most of the water entering the Faroe Shetland Channel through the FBC recirculates and returns northwestward with the current on the Faroe Plateau side. In the numerical model, a seasonal signal similar to that observed in the transport across the sill and in the periodicity of the observations is apparent in the upper layer current (u_{up}), extracted at the virtual mooring M. At M, u_{up} increases from nil in summer to 0.1 m s^{-1} in late autumn (Fig. 4g).

The changing characteristics of the observed oscillations coincide with the variability in the upper layer circulation. The observed vertical mean current between 150 and 500 m depth (i.e. well above the plume; Ullgren et al., 2015) at S3 is shown in Fig. 8a as progressive vector diagram and in Fig. 8b as vectors giving the mean velocity during T1–6. Above the plume, the velocity profiles show little variability in the vertical, suggesting a barotropically-forced current. The direction of the u_{up} changes dramatically from northeastward in T1 to southeastward in T2 and northward in T3. During intervals T2, T4 and T6 the mean upper layer current has a component directed towards the sill (i.e. opposing the dense overflow). The intervals with sill-ward flow are associated with anomalous inflow at the sill at depths shallower than 250–350 mab, and relatively weak outflow at FB (Fig. 5d). Geostrophic velocity anomalies calculated from satellite altimetry for the period and the region of interest are shown in Fig. 8c–h. Geostrophic current anomalies during T2, T4 and T6 are directed towards the sill, in fair agreement with the observations from S3 and FB.

There is no significant correlation between the along slope current in the upper layer at S3 and the transport across the sill, but upon inspection of Figs. 3, 5 and 8, a pattern emerges whereby low amplitude, long period or irregular oscillations occur when the mean upper layer current is sill-ward while energetic, relatively regular and shorter period oscillations occur when the mean upper layer current is transverse to the dense overflow. The properties of the oscillations and the plume during T1–6 are summarized in Table 3.

3.5 Barotropic forcing of the FBC outflow

The results presented in Sect. 3.4 suggest a relationship between the overflow transport variability and the local barotropic forcing on intra-seasonal time scales. The seasonal variability in the transport of dense water through the FBC has previously been linked to the seasonality in the inflow of Atlantic water towards the Nordic Seas through the FSC (Lake and Lundberg, 2006). Figure 9a shows the combinations of grid points from the AVISO gridded Sea Level Anomaly (SLA) data set, for which sea level differ-

ence ΔSLA correlates with a correlation coefficient greater than 0.65 with the transport across the FBC sill (all possible combinations of grid points within the area shown have been tested). High transport values coincide with high SLA on the Faroe Plateau and low SLA above the slope, i.e. with a geostrophically balanced barotropic current aligned with the slope and the dense outflow. The time series of ΔSLA between the combination of grid points giving the highest correlation with the transport is shown in Fig. 9b. A correlation of 0.71 indicates that about 50 % of the variance can be explained by the local barotropic forcing. Variability in ΔSLA with typical amplitudes of 0.1 m and time scales of 2–4 weeks coincides with the variability in transport, which has an amplitude of about 0.5 Sv. Linear regression gives $\Delta Q = k \Delta$SLA where $k = 6.5\,\mathrm{Sv\,m}^{-1}$. A sea level difference of 0.1 m between these two points, located 145 km a part, would give a mean barotropic current of about $0.05\,\mathrm{m\,s}^{-1}$, roughly corresponding to a change in transport across the sill on the order of 0.15 Sv (assuming a cross sectional area for the outflow of about $15\,\mathrm{km} \times 200\,\mathrm{m}$). The sensitivity obtained from the linear regression of ΔSLA against Q is four times higher (an increase in ΔSLA of 0.1 m corresponds to an increase in Q of 0.65 Sv) suggesting that the barotropic current is more focused and thus stronger in the sill region than above the Iceland-Faroe slope. Indeed, the agreement in sensitivity between ΔSLA and Q for points located more directly across the sill is better (with a factor of two). Note that with the kinematic definition of plume thickness used in the estimate of Q from FB, a barotropic current would not only influence the outflow velocity, but also the plume thickness. For the mean velocity profile from FB, the increase in kinematic interface height caused by a barotropic current of $0.1\,\mathrm{m\,s}^{-1}$ is 6 m, or approximately 3 % of the typical plume thickness.

4 Discussion

Recent results from a semi-idealized numerical model suggest that the eddies or oscillation observed downstream of the FBC sill are caused by growing baroclinic instabilities on the deeper edge of the dense plume (Guo et al., 2014). Stability analysis of

a parabolic shaped plume on a sloping bottom using the model developed by Reszka et al. (2002) and parameters relevant for the FBC overflow (Guo et al., 2014) yields that the period and wavelength of the most unstable wave decrease and the growth rate increase with increasing plume thickness (Fig. 10a). These results are in agreement with the observations presented in Sect. 3. The oscillation period decreases for increasing transport across the sill and a thicker plume and, while there are exceptions, the EKE tends to be high when the plume is thick and the volume transport is large (e.g. August and April), and low when the plume is thin and the volume flux is low (e.g. November). The link between the plume thickness, BC and EKE is even more obvious in the realistically forced numerical model, and the same tendency was observed in the experiments of Guo et al. (2014). The dominant period and the transport across the sill are obtained for the five sensitivity runs discussed in Guo et al. (2014) and the results are included in Fig. 6. Note that the forcing – and thus the transport and also the oscillation period is quasi-constant for each of the runs. The sensitivity in the oscillation period to changes in transport in these, highly idealized model runs (forced solely by a dense inflow through the FSC on the northern boundary) is much smaller ($-0.6\,\mathrm{days\,Sv^{-1}}$) than in the observations and in the more realistic model setup described in this paper. Why is the oscillation period in the idealized model runs much less sensitive to the overflow transport than the observations and the realistic modeling? One possible reason is, that while the transport variability in the observations and in the realistic model to a large extent is caused by barotropic forcing (see Fig. 9) the increased flux in the idealized model is due solely to increased baroclinic forcing. In addition, the observations and the realistic model show a barotropic velocity shear (Fig. 7) in the sill region that possibly modifies the disturbances generated by the baroclinic instability (Pedlosky, 1986, p. 582–589).

The seasonally changing period observed in the realistically forced numerical model, however, does not follow the plume thickness, but rather the transport across the sill and the velocity of the upper layer. The latter two, as suggested by Fig. 9 and discussed below, are coupled, since the upper layer flow is barotropically forced and directly mod-

ulates the flow and the transport across the sill. A barotropically forced background current aligned with the outflow across the sill increases the transport of dense water, but neither the plume thickness nor the baroclinic shear through which the baroclinic instabilities grow would be affected locally. Further downstream, however, where the barotropic forcing disappears or weakens (e.g. as the barotropic current follows the shelf break to the northwest) the plume thickness and/or the baroclinic shear must be altered in order to maintain the increased transport of dense water along the slope. Thus, we expect an increased barotropic forcing at the sill to alter the conditions for baroclinic instability downstream and hence the intrinsic period of the most unstable wave. At the same time, a barotropically forced flow aligned with the plume path will influence the period *observed* at a stationary mooring, since $T_{obs} = \lambda/(c+v)$, where λ is the wavelength, c the phase velocity and v component of the background (barotropic) current that is aligned with the phase velocity. T_{obs} decreases if the mean flow is in the direction of the phase speed of the wave and increase if the current is oppositely directed (see Fig. 10c). Throughout the year, the modeled upper layer velocity in the along-slope direction at M increases from nil to $u_{up} = 0.1\,\mathrm{m\,s^{-1}}$ (Fig. 4f) and for a typical wavelength-wave number pair obtained from the instability analysis (Reszka et al., 2002; Guo et al., 2014) the corresponding reduction in the observed periodicity would be about 1 day (Fig. 10c), possibly explaining most of the variability in the period in the model results (Fig. 4d).

The results by Reszka et al. (2002) suggest that baroclinic instabilities appear as an amplifying topographic Rossby wave (TRW) in the upper layer of a two-layer flow with a continuously stratified upper layer. The observations described in Darelius et al. (2011) and Darelius et al. (2013) are consistent with TRWs. For such waves, and for the parameters relevant in the FBC (Darelius et al., 2011), the dispersion relation is given by $\omega = sN\sin\alpha$, where $s = 0.01$ is the slope, $N = 3 \times 10^{-3}\,\mathrm{s^{-1}}$ the average buoyancy frequency in the deepest 400 m and α the angle of the wave number vector from down-slope (Rhines, 1970). An estimate of α can be obtained from the principal axis of the motion, which is normal to the wave number vector if all the variance in the

Title Page

Abstract | Introduction

Conclusions | References

Tables | Figures

|◄ | ►|

◄ | ►

Back | Close

Full Screen / Esc

Printer-friendly Version

Interactive Discussion

velocity is caused by the wave motion. According to the dispersion relation, the transverse motions of the waves changes from along-slope orientation for low-frequency waves to increasingly cross-slope orientation at higher frequencies (Pickart and Watts, 1990). We would thus expect the fraction of the EKE in the cross slope component, $\beta_v = \mathrm{EKE}_v/\mathrm{EKE}$, to decrease during time periods with a longer oscillation period, and increase with a shorter oscillation period. Time series of β_v is calculated from levels above the plume at S3 and shown in Fig. 11. Consistent with theory, there is a tendency for low values of β_v during time periods with longer oscillations, e.g. in November and May. This suggest that the variability in the observed oscillation period is (at least partly) due to changes in the intrinsic period and not (only) to variable upper layer velocities and advection.

The regular oscillations observed by Geyer et al. (2006) change character towards the end of their measurement period; in October the period increases from 88 h to more than 5 days and towards the very end of the record the oscillations seemingly disappear (see their Fig. 9). The disappearance coincides with a relatively strong geostrophic velocity anomaly directed towards the sill (not shown). In a similar manner, the oscillations on the slope change character in the beginning of June 2008, as discussed by Darelius et al. (2011). This occurs when the geostrophic velocity anomaly (inferred from AVISO) changes from being mainly aligned with the dense outflow (Fig. 12a) to a situation with relatively strong southeastward flow above the lower part of the slope (Fig. 12b). It was shown that the changing oscillations on the slope in 2012/13 were associated with inflow anomalies above the outflow at the sill (Fig. 5d), similar (but weaker) anomalies are observed at FB in October and November 1999 and in June 2008 (when the oscillations in respectively Geyer et al., 2006 and Darelius et al., 2011 change character).

The inflow in the upper layer on the Faroe Bank side is generally weaker in the numerical model, and strong inflow (weak outflow) events apparent in the sill moorings (e.g. in November–December 2008, not shown) are absent or only weakly represented in the model. The failure to capture these inflow events are likely the reason for the

more regular oscillations in the numerical model compared to the observations (i.e. the smoothness of Fig. 4d compared with Fig. 3d). The brief increase in oscillation period in the modeled time series during March 2009, coincides with a weak (relative to the observations) inflow event.

The baroclinic instabilities grow fastest once the dense water exits the channel onto the open slope (high BC values in Fig. 2). The oscillations, however, are present already at the sill; Saunders (1990) describes observation of oscillations with a period of 3–6 days in the sill region and the EKE in the numerical model show elevated values on the FB side of the sill (Fig. 2d). Model results by Guo et al. (2014, see their Fig. 3) and Seim et al. (2010) show fluctuations in plume transport also at the sill. During the period with concurrent measurements at FB and the slope, the EKE at the sill broadly follows that on the slope (Fig. 3), although energy levels are much lower (the annual mean is about $100\,\mathrm{cm^2\,s^{-2}}$ in the upper layer compared to $300\,\mathrm{cm^2\,s^{-2}}$ at S3, not shown). The dense outflow across the FBC-sill shows a maximum during the summer months (June–September) and a minimum during winter (December–March, Hansen and Østerhus, 2007, their Fig. 23) that is linked to the seasonality in the inflow of Atlantic water towards the Nordic Seas through the FSC; the barotropically forced northeastward flow modulates the southwestward flow of dense waters at depth which is feeding the FBC overflow (Lake and Lundberg, 2006). The thickness of the outflow across the sill (defined as the level where the velocity is 50 % of the maximum velocity) shows a similar seasonal variability (Hansen and Østerhus, 2007) and following the results from Reszka et al. (2002), we would expect the EKE to show the same pattern. This is not observed. The mean seasonal signal in EKE from the measurements at FB shows a distinct minimum in October–December, when values are about 40 % lower than in March (Fig. 13). It is possible, that other processes influence the EKE levels observed at the sill and that they do not reflect the EKE further downstream.

The observations presented here support the conclusion by Guo et al. (2014) that the observed oscillations are caused by growing baroclinic instabilities. It has been suggested that variability in velocity records with similar time scales in mooring records

from the southwestern slope of the Faroe Shetland Channel (Hosegood and Haren, 2004) would be linke to atmospheric forcing and the generation of continental shelf waves (Hosegood and Haren, 2006; Gordon and Huthnance, 1987). Analysis of wind data from a weather station in Torshavn shows no spectral peak around four days (not shown). The wind EKE in the 2–6 days band (Fig. 14) shows a maximum in winter (when EKE in the mooring data is low) and a minimum in summer (when EKE in the mooring data is high) indicating that the observed variability in the plume region is not atmospherically forced. There is no change in the prevailing wind direction during strong (wind speed exceeding $10\,\mathrm{m\,s^{-1}}$) wind events in summer and winter. Therefore, we conclude that the observed oscillations are not atmospherically driven.

There are examples of topographic waves trapped around islands (see e.g. Brink, 1999), but analysis of mooring records from the Nordic WOCE (World Ocean Circulation Experiment) mooring arrays surrounding the Faroe Islands does not show the presence of such waves (in the frequency range observed here) in the area (Hátún, 2004) and there are no such waves in the numerical model (not shown).

5 Conclusions

Observations from the plume region downstream of the FBC sill typically show quasi-regular oscillations associated with dense domes of overflow water moving along the Iceland-Faroe slope. The first year-long mooring records from the area reveal variability in the strength and periodicity of the oscillations that are directly linked to the variability in the volume transport of dense water across the FBC. In agreement with results from the baroclinic instability theory, the oscillations are more intense with a shorter period when the volume transport and the plume thickness increase. The intra-seasonal variability in the transport across the sill is shown to be caused by variability in the local barotropic forcing. It is shown that part of the variability (order one day) in the observed oscillation period can be explained by advective effects (due to a background barotropic current), but changes in the fraction of the EKE that is caused by across

FBC variability

E. Darelius et al.

isobath motion also points to a contribution from changes in the intrinsic periodicity of the generated instabilities. The more energetic, short period oscillations are found to, to a greater extent than the long period oscillation, bring cold plume water both to the shallowest and to the deepest mooring on the slope.

References

Amante, C. and Eakins, B. W.: ETOPO1 1 Arc-Minute Global Relief Model: Procedures, Data Sources and Analysis, Tech. rep., NOAA, technical memorandum NESDIS NGDC-24, 19 pp., 2009. 829

Bishop, S. P., Watts, D. R., and Donohue, K. A.: Divergent eddy heat fluxes in the Kuroshio extension at 144°–148° E. Part I: Mean structure, J. Phys. Oceanogr., 43, 1533–1550, doi:10.1175/JPO-D-12-0221.1, 2013. 830

Bleck, R.: An oceanic general circulation model framed in hybrid isopycnic-Cartesian coordinates, Ocean Model., 37, 55–88, 2002. 829

Brink, K. H.: Island-trapped waves, with application to observations off Bermuda, Dynam. Atmos. Oceans, 29, 93–118, doi:10.1016/S0377-0265(99)00003-2, 1999. 840

Cappelen, J.: Technical Report 14-09: Weather observations from Tórshavn, The Faroe Islands, Tech. rep., Danish Meterological Institute, Copenhagen, available at: http://www.dmi.dk/fileadmin/Rapporter/TR/tr14-09, 2014. 829, 861

Chassignet, E. P., Hurlburt, H. E., Smedstad, O. M., Halliwel, G. R., Hogan, P. J., Wallcraft, A. J., Baraille, R., and Bleck, R.: The HYCOM (HYbrid Coordinate Ocean Model) data assimilative system, J. Marine Syst., 65, 60–83, 2007. 829

Darelius, E., Smedsrud, L. H., Østerhus, S., Foldvik, A., and Gammelsrød, T.: Structure and variability of the Filchner overflow plume, Tellus A, 61, 446–464, doi:10.1111/j.1600-0870.2009.00391.x, 2009. 825

Darelius, E., Fer, I., and Quadfasel, D.: Faroe Bank Channel overflow: mesoscale variability, J. Phys. Oceanogr., 41, 2137–2154, doi:10.1175/JPO-D-11-035.1, 2011. 825, 826, 831, 837, 838

Darelius, E., Ullgren, J. E., and Fer, I.: Observations of barotropic oscillations and their influence on mixing in the Faroe Bank Channel overflow region, J. Phys. Oceanogr., 43, 1525–1532, doi:10.1175/JPO-D-13-059.1, 2013. 825, 826, 830, 831, 837

Dee, D. P., Uppala, S. M., Simmons, A. J., Berrisford, P., Poli, P., Kobayashi, S., Andrae, U., Balmaseda, M. A., Balsamo, G., Bauer, P., Bechtold, P., Beljaars, A. C. M., van de Berg, L., Bidlot, J., Bormann, N., Delsol, C., Dragani, R., Fuentes, M., Geer, A. J., Haimberger, L., Healy, S. B., Hersbach, H., Hólm, E. V., Isaksen, L., Kållberg, P., Köhler, M., Matricardi, M., McNally, A. P., Monge-Sanz, B. M., Morcrette, J.-J., Park, B.-K., Peubey, C., de Rosnay, P., Tavolato, C., Thépaut, J.-N., and Vitart, F.: The ERA-Interim reanalysis: configuration and performance of the data assimilation system, Q. J. Roy. Meteor. Soc., 137, 553–597, doi:10.1002/qj.828, 2011. 829

Dickson, R. R. and Brown, J.: The production of North Atlantic deep water, sources, rates, and pathways, J. Geophys. Res., 99, 12319–12341, doi:10.1029/94JC00530, 1994. 825

Fer, I., Voet, G., Seim, K. S., Rudels, B., and Latarius, K.: Intense mixing of the Faroe Bank Channel overflow, Geophys. Res. Lett., 37, L02604, doi:10.1029/2009GL041924, 2010. 825

Geyer, F., Østerhus, S., Hansen, B., and Quadfasel, D.: Observations of highly regular oscillations in the overflow plume downstream of the Faroe Bank Channel, J. Geophys. Res., 111, 1–11, doi:10.1029/2006JC003693, 2006. 825, 831, 838

Gordon, R. L. and Huthnance, J.: Storm-driven continental shelf waves over the Scottish continental shelf, Cont. Shelf Res., 7, 1015–1048, 1987. 840

Title Page

Abstract | Introduction

Conclusions | References

Tables | Figures

◀ | ▶▶

◀ | ▶

Back | Close

Full Screen / Esc

Printer-friendly Version

Interactive Discussion

Guo, C., Ilicak, M., Fer, I., Darelius, E., and Bentsen, M.: Baroclinic instability of the Faroe Bank Channel overflow, J. Phys. Oceanogr., 44, 2698–2717, doi:10.1175/JPO-D-14-0080.1, 2014. 825, 830, 835, 836, 837, 839

Hansen, B. and Østerhus, S.: Faroe Bank Channel overflow 1995–2005, Prog. Oceanogr., 75, 817–856, 2007. 825, 828, 830, 832, 833, 839, 848, 852

Hansen, B., Turrell, W. R., and Østerhus, S.: Decreasing overflow from the Nordic seas into the Atlantic Ocean through the Faroe Bank Channel since 1950, Nature, 411, 927–930, 2001. 830

Hosegood, P. and Haren, H. V.: Near-bed solibores over the continental slope in the Faeroe-Shetland Channel, Deep-Sea Res. Pt. II, 51, 2943–2971, doi:10.1016/j.dsr2.2004.09.016, 2004. 840

Hosegood, P. and Haren, H. V.: Sub-inertial modulation of semi-diurnal currents over the continental slope in the Faeroe-Shetland Channel, Deep-Sea Res, Pt. I, 53, 627–655, doi:10.1016/j.dsr.2005.12.016, 2006. 840

Høyer, J. L. and Quadfasel, D.: Detection of deep overflows with satellite altimetry, Geophys. Res. Lett., 28, 1611–1614, 2001. 825

Hátún, H.: The Faroe Current (Ph.D. thesis), Tech. rep., University of Bergen, Bergen, 2004. 840

Krauss, W. and Käse, R. H.: Eddy formation in the Denmark Strait overflow, J. Geophys. Res.-Oceans, 103, 15525–15538, 1998. 825

Lake, I. and Lundberg, P.: Seasonal barotropic modulation of the deep-water overflow through the Faroe Bank Channel, J. Phys. Oceanogr., 36, 2328–2339, doi:10.1175/JPO2965.1, 2006. 834, 839

Large, W. G., McWilliams, J. C., and Doney, S. C.: Oceanic vertical mixing: a review and a model with a nonlocal boundary layer parametrization, Rev. Geophys., 32, 363–403, 1994. 829

Mauritzen, C., Price, J., Sanford, T., and Torres, D.: Circulation and mixing in the Faroese Channels, Deep-Sea Res. Pt. I, 52, 883–913, doi:10.1016/j.dsr.2004.11.018, 2005. 825, 828, 830

Miller, A. J., Lermusiaux, P. F. J., and Poulain, P.-M.: A topographic–Rossby mode resonance over the Iceland–Faeroe Ridge, J. Phys. Oceanogr., doi:10.1175/1520-0485(1996)026<2735:ATMROT>2.0.CO;2, 1996. 825

Mysak, L. A. and Schott, F.: Evidence for baroclinic instability of the Norwegian current, J. Geophys. Res., 82, 2087, doi:10.1029/JC082i015p02087, 1977. 825

Title Page

Abstract | Introduction

Conclusions | References

Tables | Figures

|◀ | ▶|

◀ | ▶

Back | Close

Full Screen / Esc

Printer-friendly Version

Interactive Discussion

Pedlosky, J.: Geophysical Fluid Dynamics, 2nd edn., Springer Verlag, 1986. 836

Pickart, R. S. and Watts, D. R.: Deep western boundary current variability at Cape Hatteras, J. Mar. Res., 48, 765–791, doi:10.1357/002224090784988674, 1990. 838

Rasmussen, T. A., Olsen, S. M., Hansen, B., Hátún, H., and Larsen, K. M.: The Faroe shelf circulation and its potential impact on the primary production, Cont. Shelf Res., 88, 171–184, doi:10.1016/j.csr.2014.07.014, 2014. 826, 830

Reszka, M. K., Swaters, G. E., and Sutherland, B. R.: Instability of abyssal currents in a continuously stratified ocean with bottom topography, J. Phys. Oceanogr., 32, 3528–3550, 2002. 836, 837, 839

Rhines, P. B.: Edge-, bottom-, and Rossby waves in a rotating stratified fluid, J. Fluid Mech., 69, 273–302, 1970. 837

Saunders, P. M.: Cold outflow from the Faroe Bank Channel, J. Phys. Oceanogr., 20, 29–43, 1990. 839

Seim, K. S., Fer, I., and Berntsen, J.: Regional simulations of the Faroe Bank Channel overflow using a σ-coordinate ocean model, Ocean Model., 35, 31–44, doi:10.1016/j.ocemod.2010.06.002, 2010. 826, 839

Simonsen, K., Larsen, K. M. H., Mortensen, L., and Norbye, A. M.: New Bathymetry for the Faroe Shelf, Tech. rep., Faculty of Science and Technology, University of the Faroe Islands, 2002. 829

Skagseth, Ø. and Orvik, K. A.: Identifying fluctuations in the Norwegian Atlantic slope current by means of empirical orthogonal functions, Cont. Shelf Res., 22, 547–563, doi:10.1016/S0278-4343(01)00086-3, 2002. 825

Torrence, C. and Compo, G. P.: A practical guide to wavelet analysis, B. Am. Meteorol. Soc., 79, 61–78, doi:10.1175/1520-0477(1998)079<0061:APGTWA>2.0.CO;2, 1997. 827

Ullgren, J., Darelius, E., and Fer, I.: Faroe Bank Channel overflow in one year of mooring measurements at the exit of the channel, Ocean Sci., in preparation, 2015. 826, 827, 834, 848

Voet, G. and Quadfasel, D.: Entrainment in the Denmark Strait overflow plume by meso-scale eddies, Ocean Sci., 6, 301–310, doi:10.5194/os-6-301-2010, 2010. 826

Title Page

Abstract | Introduction

Conclusions | References

Tables | Figures

|◀ | ▶|

◀ | ▶

Back | Close

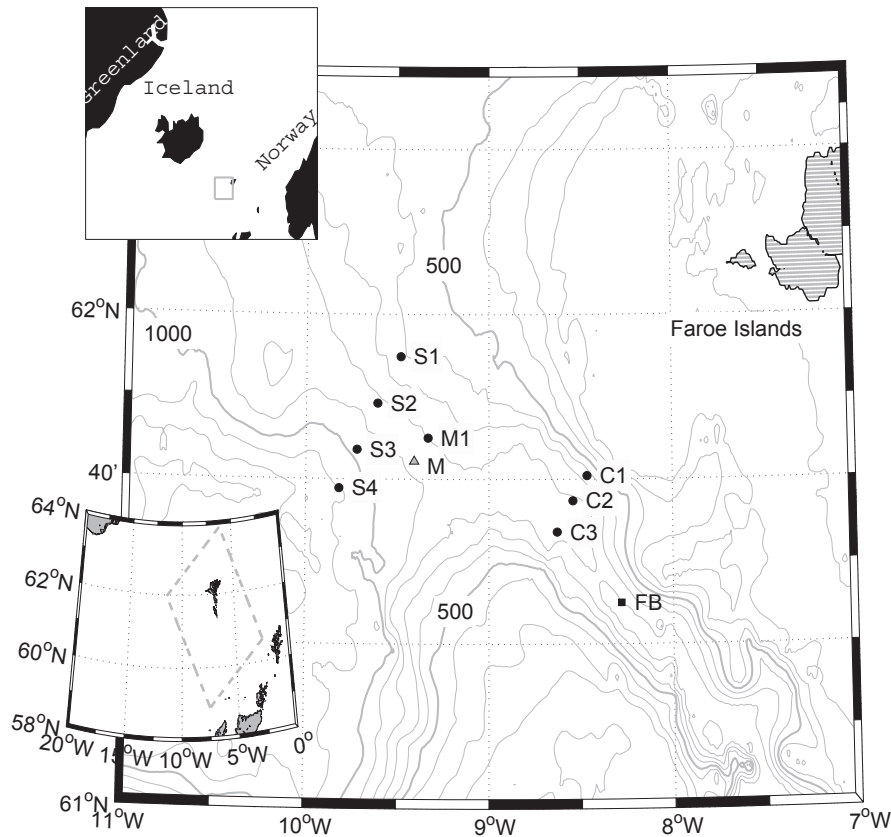Full Screen / Esc

Printer-friendly Version

Interactive Discussion

Table 1. Details of the moorings deployed 28 May 2012 to 5 June 2013 downstream of the FBC sill. For instrumentation, the target height above bottom (in meters above bottom, mab) is given. RCM is Anderaa Recording Current Meter, SBE is Seabird, ADCP is Acoustic Doppler Current Profiler. The interval given in the ADCP-column shows the depth range (in mab) for which velocity measurements are obtained. Superscripts indicate the following: asterisks indicate that conductivity is measured, U that the ADCP is upward looking, s that the record is only 3 months long and A that a Nortek Aquadopp is used.

	Longitude (W)	Latitude (N)	Depth [m]	RCM	SBE37*/39/56	ADCP
C1	8°27.9′	61°40.43′	650	–	10/30/40/50/60/80 100*/125/150/200*	20–200
C2	8°32.54′	61°37.4′	807	27[A]	25*/50/75/100*/125/150 175/200/250*/300/350	30–370
C3	8°37.7′	61°33.6′	859	25	27*/100*/140	20–140
S1	9°28.98′	61°54.87′	610	80	–	–
S2	9°36.54′	61°49.2′	805	25	27*/50/75/100*/150 175/200*/250	35–260
S3	9°43.22′	61°43.59′	950	25	27*/50/100*/125/150/200 250*/300/350/400/450/500*	20–470, 520–820[U]
S4	9°49.1′	61°38.89′	1082	25/75 150/300	27*50/100*/125/175 250*/300/350/400/450/500*	–
M1	9°19.97′	61°45.01′	808	25	27*/50/75/100/125/150 170*/200/250/300	70–170[s]

Table 2. Definition of time intervals T1–6. Dates are given in the format dd/mm/yy.

	Interval	Duration [days]
T1	01/06/12–01/09/12	92
T2	02/09/12–19/10/12	48
T3	20/10/12–09/11/12	21
T4	10/11/12–29/11/12	20
T5	30/11/12–20/04/13	142
T6	21/04/12–05/06/13	46

Table 3. Plume and oscillation characteristics during T1–6. Plume thickness is the mean height of the 6 °C isotherm at S2 ± the SD. Plume transport is the period mean transport obtained from FB. S1/S4 gives the percentage of time that the deepest instrument on the S1 and S4 mooring is surrounded by water colder than 3 °C. Upper layer velocity is the along slope velocity from S3, 700 mab ± the SD of the low passed velocity records shown in 5c.

	Oscillation period [days]	Plume thickness [m]	Plume transport [Sv]	S1/S4 [%]	Upper layer velocity [cm s^{-1}]
T1	3–4	108 ± 39	2.3	15/23	1 ± 1
T2	6	102 ± 29	2.0	6/ 8	-7 ± 1
T3	6	97 ± 33	1.9	7/1	5 ± 1
T4	–	84 ± 10	1.5	0/0	-3 ± 0
T5	3–4/6	97 ± 35	2.2	11/26	0 ± 1
T6	6/–	89 ± 20	1.7	2/1	-2 ± 0

Figure 1. Map showing the study region. Isobaths are shown every 100 m (thin, grey lines) and every 500 m (thick, gray lines). The locations of the moorings are indicted by black, labeled circles (Ullgren et al., 2015) and squares (Hansen and Østerhus, 2007). The location of the virtual mooring "M" (extracted from the model) is shown by the gray triangle. The upper inset shows the location of the study region (gray box) and the lower inset the model domain (dashed, gray box).

Title Page

Abstract | Introduction

Conclusions | References

Tables | Figures

|◄ | ►|

◄ | ►

Back | Close

Full Screen / Esc

Printer-friendly Version

Interactive Discussion
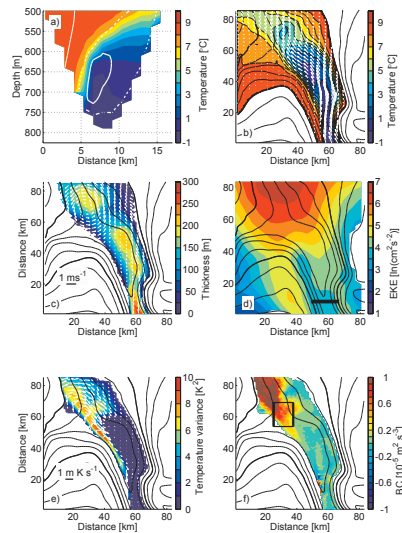
Figure 2. Modeled fields: **(a)** Temperature (color) and outflow velocity (white contours) at a section across the sill (thick black line in **(d)**). The 0/0.5/1 m s^{-1} contours are marked with a thin/dotted/thick white line. **(b)** Mean temperature (color) and velocity at 100 mab (white arrows). **(c)** Snapshot of plume thickness (color) and velocity at 500 m depth from 12 August 2008 at 01:00 UTC. The velocity scale given by the thick black line is valid for panel **(b, c)**. **(d)** Annual mean eddy kinetic energy (EKE, color) at 300 m depth. Note that the color scale is logarithmic. The thick black line indicates the position of the section shown in **(a)**. **(e)** Temperature variance (color) and divergent eddy heat flux (EHT, white arrows) at 100 mab. **(f)** Baroclinic conversion rate (BC, color). The black box shows the region used to calculate time series of BC shown in Fig. 4f. In panels **(b–f)**, the bathymetry is shown every 100 m (thin, black lines) while the 500 and 1000 m isobaths are indicated by a thick, black line. If not otherwise stated, the data shown are mean fields from August 2008. Only data from regions where the mean plume thickness is larger than 50 m is included in **(e, f)**. For clarity, only data below 500 m depth is included in **(b)**.
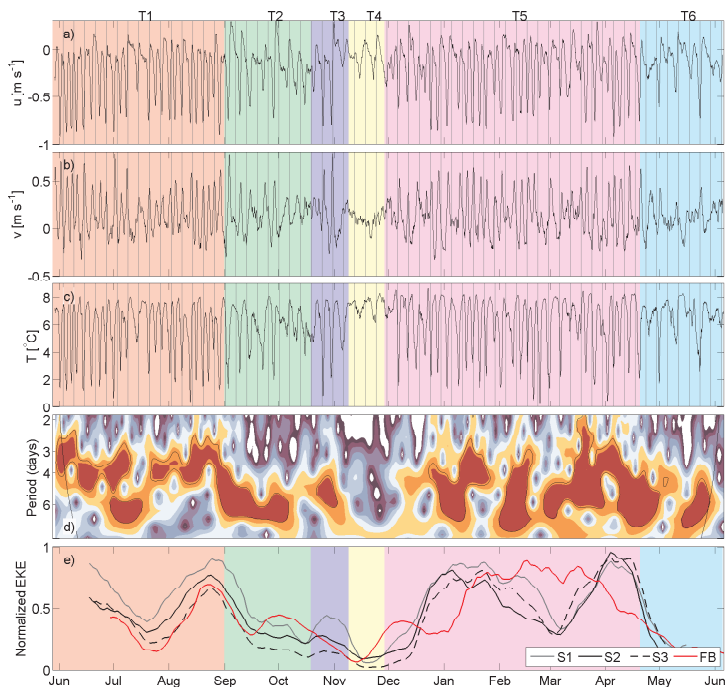
Figure 3. Time series from observations of **(a)** along-slope velocity, u, **(b)** across-slope velocity, v, and **(c)** temperature, T measured at 80 mab at mooring S1. Thin gray lines are inserted every 6th days and the background color identifies the time intervals T1–6 marked in **(a)** and discussed in the text. **(d)** Results from wavelet analysis of along slope velocity, measured at 600 mab at mooring S3. Red colors indicate high energy levels and the black line the 95 % confidence levels. Results before and after the thin black lines at the start and end of the record are affected by edge effects. **(e)** Vertical mean EKE at moorings on the slope and the sill according to the legend. Values are normalized by the maximum value at each mooring.
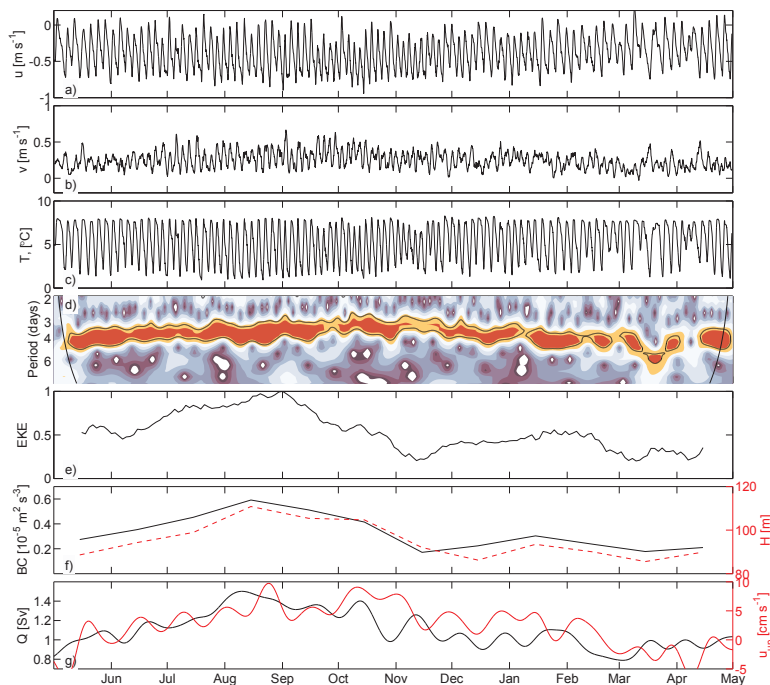
Figure 4. Modeled time series of **(a)** velocity, u, **(b)** velocity, v, and **(c)** temperature, T, at 100 mab at the virtual mooring M (see Fig. 1 for location). **(d)** Wavelet analysis of record shown in **(a)**. Red colors indicate high energy and the black line the 95 % significance level. Results before and after the thin black lines at the start and end of the record are affected by edge effects. **(e)** Vertical mean EKE from M, normalized by its maximum value. **(f)** Time series of baroclinic conversion rate (BC, black line) and mean plume thickness (dashed, red line), monthly mean values from the box shown in Fig. 2f. **(g)** Transport across the sill (black line) and mean velocity in the along slope direction in the upper layer (100–300 m) at M (red line).
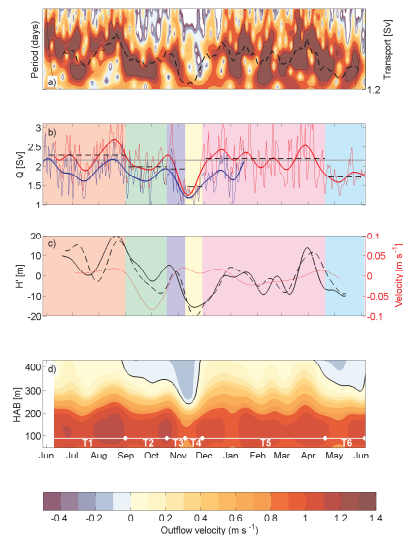
Figure 5. Time series from observations. **(a)** Results from the wavelet analysis of the along slope velocity, S3 600 mab. Red colors indicate high energy levels and the black line the 95 % confidence levels. Dashed line (right axis) is the transport estimate from FB. **(b)** Transport estimates based on data from array C (blue) and at the sill from FB at the sill (red). Thin lines are daily means and thick lines show the low passed time series. The dashed lines show mean values from FB during time interval T1–6 discussed in the text and indicated in the background by colors. The gray line shows the mean value from the sill for the period 1995–2005 (Hansen and Østerhus, 2007). **(c)** Plume thickness anomaly ($H' = H - \bar{H}$, where the bar denotes the time mean value) at S2 (black, dashed) and S3 (black, full) and upper layer (500–700 mab) velocity in the along slope direction at S3 (red). The data are low pass filtered (30 days). Plume thickness is defined as the height above bottom of the 6°C isotherm. **(d)** Observed outflow velocity at FB in June 2012–May 2013, where positive values (red colors) indicate flow towards the North Atlantic (outflow). The black line shows the zero isotach and the white line intersected by white circles shows the time intervals introduced in Fig. 3 and discussed in the text.
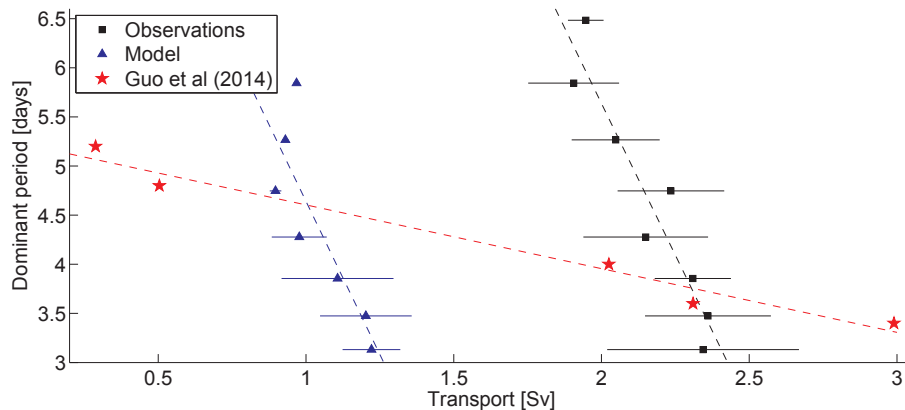
Figure 6. Mean transport across the sill averaged in time periods with different dominant oscillation periods approximately 80 km downstream of the sill. The dominant period is identified as the most energetic oscillation period for each time step in the wavelet analysis. The horizontal lines show the SD and the dashed lines show the results from linear regression.
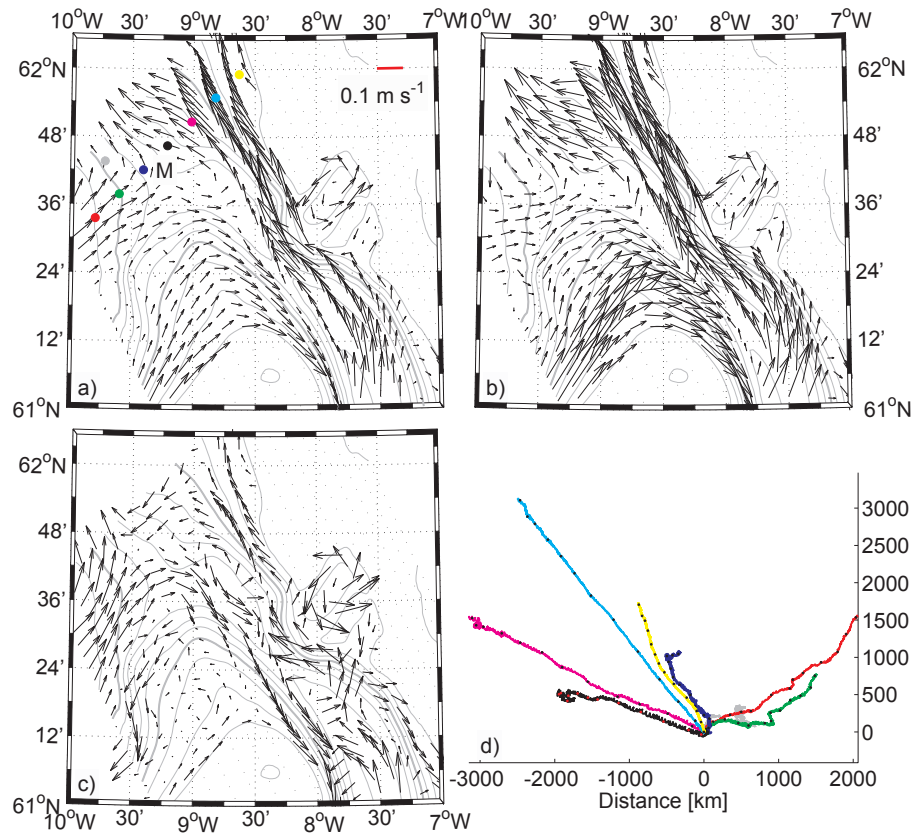
Figure 7. Modeled **(a)** annual mean currents and monthly mean currents in **(b)** August 2008 and **(c)** March 2009 at 200 m depth. Isobaths are shown every 100 m (gray, thin lines) and every 500 m (thick, gray line) and the circles indicate the origin of the data shown in **(d)**. **(d)** Progressive vector diagram of currents at locations indicated with circles of the corresponding color in **(a)**. The start of every month is marked with a black or red dot. For comparison, the upper layer currents observed at S3 (grey circle in **(a)**) is included (grey line).
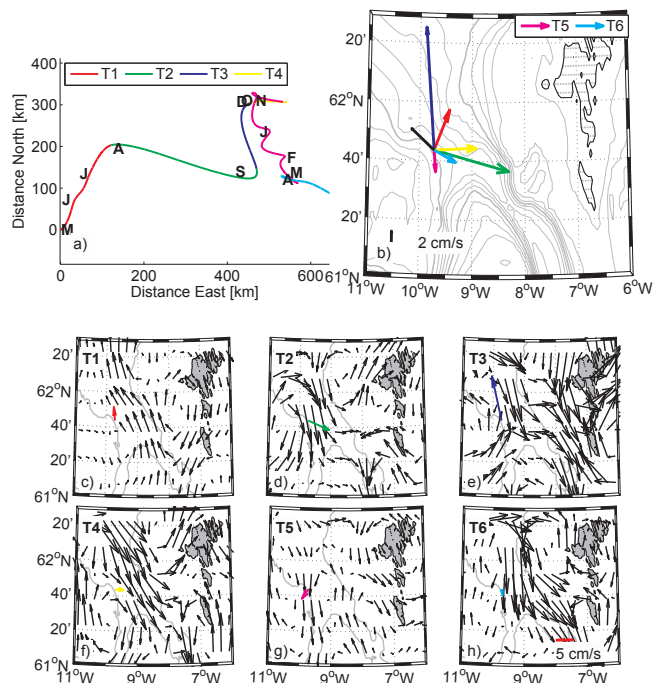
Figure 8. (a) Progressive vector diagram of upper layer velocity (u_{up}) from S3 with data from time intervals colored according to legend. **(b)** Mean velocity in the upper layer at S3 during T1–6. The velocity scale is given in the lower left corner and the black arrow at S3 shows the mean direction of the dense plume, 75 mab. Data in **(a, b)** are vertical mean values from 150 to 500 m depth. Mean geostrophic velocity anomaly (AVISO) during **(c)** T1, **(d)** T2, **(e)** T3, **(f)** T4, **(g)** T5 and **(h)** T6. The mean upper layer velocity anomaly from S3 for each period is included for reference and the velocity scale (for **c–h**) is given in the lower right corner of **(h)** as a labeled red line.
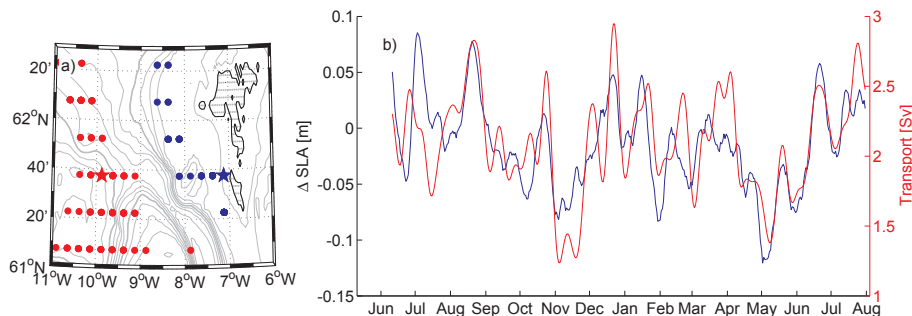
Figure 9. (a) Map over the study region showing the grid points from the AVISO gridded data set of sea level anomalies (SLA) from 2012/13 where the difference in SLA (ΔSLA) between any of the blue circles and (at least) one of the red circles correlates positively with the transport across the sill and where $r > 0.65$. The stars indicate the grid point combination with the highest correlation ($r = 0.71$) and the corresponding time series of ΔSLA is shown in **(b)** (blue line) together with the transport across the sill from FB (red line). All data are 14 days low passed filtered.
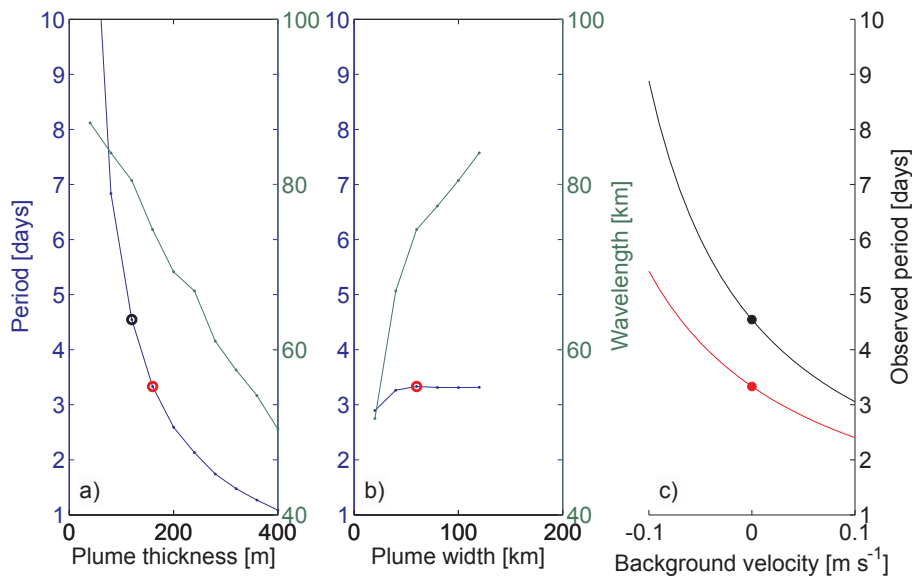
Figure 10. Period (blue) and wavelength (green) of the most unstable wave as a function of **(a)** plume thickness (plume width = 60 km) and **(b)** plume width (plume thickness = 160 m) from Reszka's model (2002). **(c)** Period observed at a stationary mooring as a function of background current for an oscillation with the (intrinsic) period – wavelength pairs marked with a red and black circle in **(a, b)**.
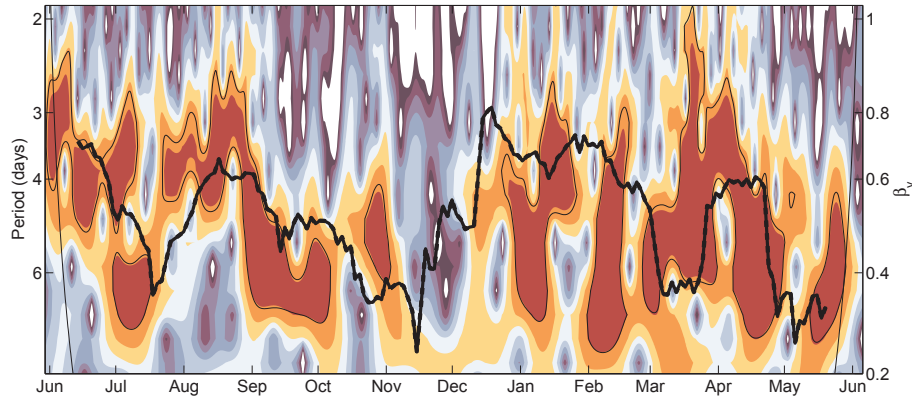
Figure 11. Time series of $\beta_v = \mathrm{EKE}_v/\mathrm{EKE}$ (thick, black line) superimposed on a wavelet diagram from S3 (same as shown in Fig. 3d). Red colors indicate high energy and the thin, black line is the 95 % significance level.
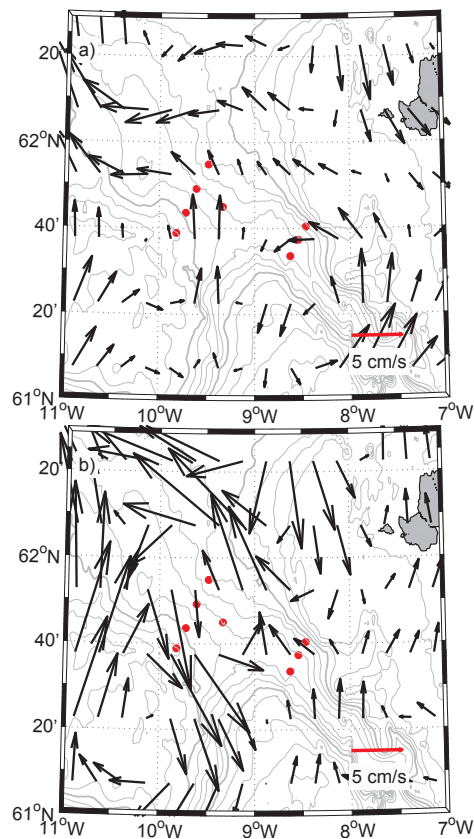
Figure 12. Mean geostrophic velocity anomaly (from AVISO) during the period **(a)** 1–31 May 2008 and **(b)** 3–10 June 2008. The red dots mark the positions of the moorings deployed 2012/13.
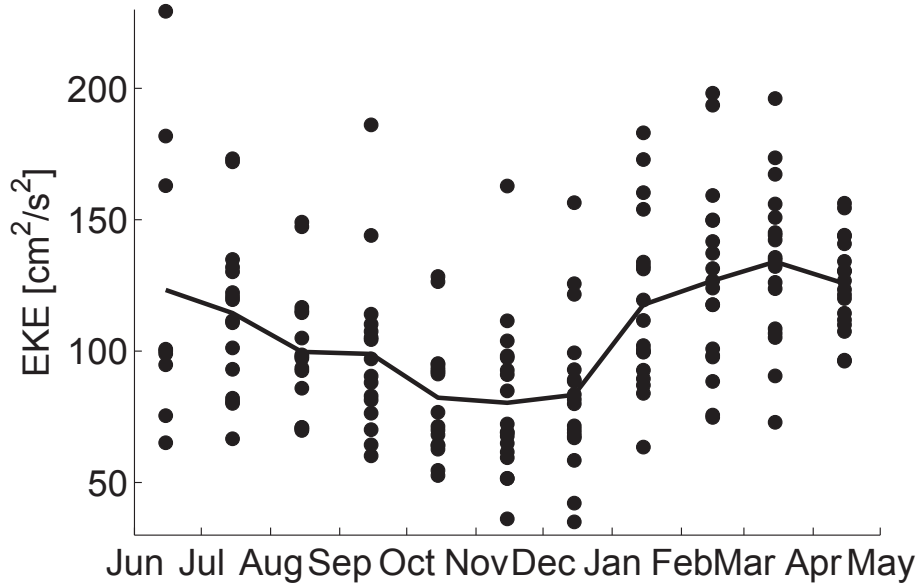
Figure 13. Monthly mean EKE at mooring FB (1995–2014, see Fig. 1 for location). Each circle represents the monthly mean from one deployment and the black line shows the mean seasonal signal.

Discussion Paper | Discussion Paper | Discussion Paper | Discussion Paper |

OSD

12, 823–861, 2015

FBC variability

E. Darelius et al.

Title Page

Abstract | Introduction

Conclusions | References

Tables | Figures

|◄ | ►|

◄ | ►

Back | Close

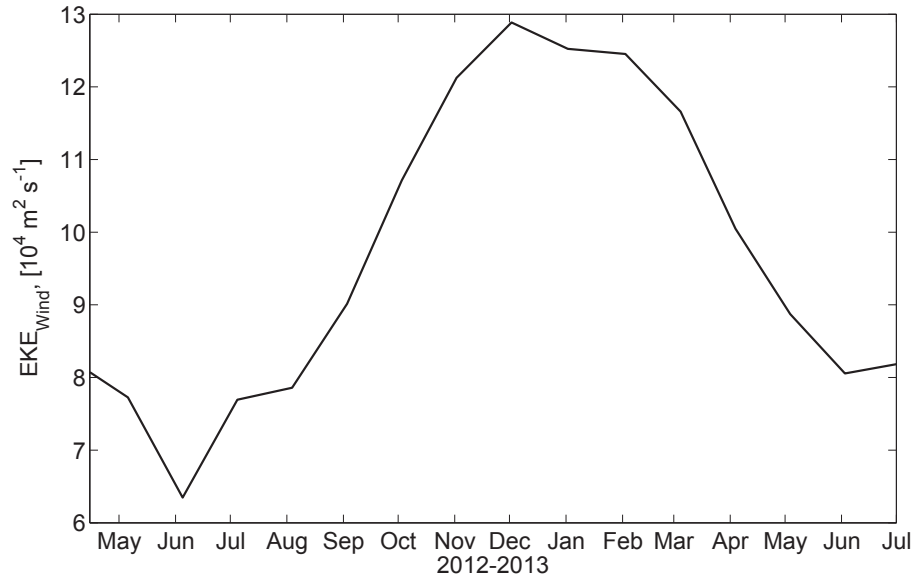Full Screen / Esc

Printer-friendly Version

Interactive Discussion

Figure 14. Time series of EKE from wind observations in Torshavn (Cappelen, 2014) during 2012/13.